A numerical investigation of central binary collision of droplets

N. Nikolopoulos [a], K.-S. Nikas [a,b], G. Bergeles [a,*]

[a] Department of Mechanical Engineering, National Technical University of Athens, 5 Heroon Polytechniou, Zografos, 15710 Athens, Greece
[b] Technological Education Institute of Piraeus, Mechanical Engineering Department, Fluid Mechanics Laboratory, 250 Thivon & P. Ralli str., Aigaleo 12244, Greece

ARTICLE INFO

ABSTRACT

The paper presents a numerical investigation of the central collision of two equal-sized droplets in a gaseous phase. The investigation is based on the numerical solution of the Navier–Stokes equations in their axi-symmetric form using the finite volume technique. The Volume of Fluid Method (V.O.F) is employed for tracking the liquid–gas interface. An adaptive local grid refinement technique developed recently is used in order to increase the resolution around the interface. By using two V.O.F indicator functions the identity of each droplet is preserved and can be detected after droplet contact until coalescence. The results are compared with available experimental data and provide a very detailed picture of the collision process, the ligament formation and dimensions, the pinch off mechanism and the creation of the satellite droplet. The conversion of the droplet's kinetic energy to the surface energy and vise versa, the energy viscous dissipation as well as the maximum deformation of the droplets are also evaluated.

© 2008 Elsevier Ltd. All rights reserved.

1. Introduction

The binary droplet collision is of importance in a variety of engineering areas, such as spray cooling, spray coating and direct fuel injection into internal combustion engine cylinders. In fact, the present research work is stimulated by the last area. Adam et al. [1], Park [2], Brazier-Smith et al. [3], Ashgriz and Poo [4] performed a series of experiments using water droplets in order to interpret the mechanisms governing cloud and raindrop growth. The collision of hydrocarbon droplets was studied by Ashgriz and Givi [5,6], who used *n*-hexane in burning and inert environments as well as Brenn and Frohn [7,8] who studied the collision and merging of two droplets of propanol-2, water and *n*-hexadecane. Willis and Orme [9] conducted experiments of droplet collisions in a vacuum, devoid of aerodynamic effects. Jiang et al. [10], focusing on spray combustion, used hydrocarbon droplets (heptane, decane, dodecane, tetradecane and hexadecane), whilst Qian and Law [11] investigated the effects of ambient pressure, density and viscosity on the evolution of the droplet collision process.

The governing non-dimensional parameters of the central binary collision phenomenon are the droplet Weber number (We) and the Reynolds number (Re). The physical criterion that determines the outcome of the collision (i.e., bouncing or coalescence) is the gap size between the droplets. A size comparable to that of the molecular interaction, typically of the order of 10^2 Å (Mackay and Mason [12] and Bradley and Stow [13]) results in coales-

cence, otherwise the droplets will bounce. The collision outcome depends also on the viscosity and density of the liquid and gas phases as well as on the surface tension, indicating the significance of the rheological properties. If the initial kinetic energy of the droplets is very low (more precisely if the droplet Weber number is very low), the droplets coalesce permanently, without bouncing, since there is sufficient time to expel the intervening gas layer, which is the barrier of coalescence (regime I). Increasing the Weber number, droplet deformation occurs and the droplets experience bouncing (regime II). If the Weber number is further increased, the droplets coalesce permanently, with a time delay depending on the Weber number. If the kinetic energy is high (i.e., high Weber number) the droplets coalesce immediately. The coalesced droplet deforms into a disk and oscillates until it relaxes to a spherical droplet due to the surface tension forces (regime III). At the transition regime IV, the collision energy overcomes the surface energy and oscillation causes the droplet to separate into two droplets. Further increasing the Weber number in regime IV makes collision energy so high, that a ligament is created between the two droplet masses that eventually breaks into two or more satellite droplets. The above description is based on the study of Qian and Law [11], who examined detailed photographs of the collision process. The present numerical predictions are assessed against their experiments. Ashgriz and Poo [4] showed that for head-on collision and large Weber number, the number of satellite droplets resulting from the droplet separation (phase IV) also increases.

Previous numerical studies by Tsamopoulos and Brown [14] and Patzek et al. [15] have focused on the nonlinear oscillations of droplets assuming an inviscid collision process. Viscous effects were investigated by both Foote [16], who used a

---

* Corresponding author. Tel.: +30 2107721058; fax: +30 2107723616.
E-mail addresses: niknik@fluid.mech.ntua.gr (N. Nikolopoulos), ksnikas@teipir.gr (K.-S. Nikas), bergeles@fluid.mech.ntua.gr (G. Bergeles).

Marker-And-Cell (MAC) method to solve the full Navier–Stokes equations as well as Lundgren and Mansour [17], who used a modified boundary integral method that accounts approximately for the small viscous dissipation effects. According to Jiang et al. [10] the energy dissipation Φ is independent of the Reynolds number (i.e., viscosity) and depends only on the Weber number. Their experiments however were limited to relatively small Weber numbers (We < 120). Recently however, Willis et al. [18] conducted experiments of droplet binary collision for 10 and 30 cS viscosity liquids in a vacuum with Weber number as high as 250. They found that the energy dissipation increased with increasing fluid viscosity. The modeling of Dai and Schmidt [19] extended the observations of Willis et al. [18] and reached the conclusion that the rate of dissipation (i.e., $\partial\Phi/\partial t$) increases with increasing viscosity, while the maximum deformation and energy dissipation decrease with increasing Reynolds number, suggesting that the effect of viscosity on the maximum deformation becomes insignificant at sufficiently high Reynolds numbers.

A variety of numerical methods have been used for the simulation of the binary droplet collision. Unverdi and Tryggvason [20–22] developed the front tracking method, Nobari et al. [23] implemented the method in axi-symmetric setting and Nobari and Tryggvason [24] extended it in three dimensions. Lafaurie et al. [25] used the SURFER method, Lattice Boltzmann models were used by Drtina et al. [26] and Schelkle and Frohn [27,28], while Rieber and Frohn [29] used the V.O.F method.

The present investigation studies numerically the central collision of two hydrocarbon droplets of equal size for various Weber and Reynolds numbers. Assuming central collision, the axi-symmetric form of the Navier–Stokes equations can be solved. The equations are discretised with the finite volume technique whilst the Volume of Fluid Method is used for the tracking of the liquid–gas interfaces. By using two V.O.F indicator functions, the identity of each droplet is preserved and can be detected after contact until coalescence (should this occur). Similar to previous studies, the time instant for droplet coalescence is provided externally, according to the respective experimental data.

2. Mathematical formulation

2.1. The V.O.F indicator function "α"

The flow induced by the central binary collision of two droplets is considered as two-dimensional axi-symmetric (as the experiments suggest for the We number considered), incompressible and laminar. The two-phase flow is mathematically expressed by the Navier–Stokes equations (that include extra terms to account for the surface tension) and the continuity equation. Phase 1 refers to the liquid phase i.e., the two droplets and phase 2 to the surrounding gas phase. For identifying each phase separately a volume fraction, denoted by "α", is introduced following the Volume of Fluid Method (V.O.F) of Hirt and Nichols [30]. The volume fraction "α" is defined as:

$$\alpha = \frac{\text{Volume of fluid1 (liquid phase)}}{\text{Total volume of the control volume}} \tag{1}$$

The values of density "ρ" and dynamic viscosity "μ" are calculated using linear interpolation between the values of the two phases weighed with the volume fraction "α" i.e.,

$$\begin{aligned}\rho &= \alpha\rho_{liq} + (1-\alpha)\rho_{gas}\\ \mu &= \alpha\mu_{liq} + (1-\alpha)\mu_{gas}\end{aligned} \tag{2}$$

where the "α"-function is equal to:

$$a(x,t) = \begin{cases} 1, & \text{for a point } (x,t) \text{ inside liquid (fluid1)} \\ 0, & \text{for a point } (x,t) \text{ inside gas (fluid2)} \\ 0 < \alpha < 1, & \text{for a point } (x,t) \text{ inside the} \\ & \text{transitional area between the two phases} \end{cases} \tag{3}$$

Following Hirt and Nichols [30], the material derivative of the V.O.F function "α" is zero i.e.:

$$\frac{\partial a}{\partial t} + \vec{u} \cdot \nabla a = 0 \tag{4}$$

The momentum equations expressing both phases are written in the form

$$\frac{\partial(\rho\vec{u})}{\partial t} + \nabla \cdot (\rho\vec{u} \otimes \vec{u} - \vec{T}) = \rho\vec{g} + \vec{f}_\sigma \tag{5}$$

where $\vec{u}$ is the velocity vector, "t" is time, $\vec{T}$ is the stress tensor and f_σ is the volumetric force due to surface tension. The value of "f_σ", following the CCS method of Brackbill et al. [32], is equal to $f_\sigma = \sigma \cdot \kappa \cdot (\nabla a)$, where σ is the surface tension (for immiscible fluids the value is always positive) and κ is the curvature of the interface region.

The V.O.F methodology has been successfully applied by Nikolopoulos et al. [31] to study the splashing of a single droplet onto a wall film. An adaptive local grid refinement technique, proposed recently by Theodorakakos and Bergeles [33] and used in Nikolopoulos et al. [34], is also employed in the present investigation in order to enhance accuracy in the areas of interest (i.e., the interface between the two phases) while reducing the computational cost. The gas–liquid interface is characterized by high flow gradients, so in order to achieve the desired level of resolution, the cells are sub-divided into a prescribed number of layers in both sides of the interface. In most cases five levels of local refinement are used. A new locally refined mesh is created every 10 time steps following the liquid–gas interface motion and distortion. As a result, the interface is always resolved by the finest mesh.

2.2. Second VOF indicator function

If a single V.O.F variable is used then, upon contact, the two droplets will immediately coalesce, which is not correct for low Weber number impact. In order to overcome this problem, a separate V.O.F variable is assigned to each droplet, i.e., "α_1" for the first droplet and "α_2" for the second. Consequently each droplet is separately tagged thus eliminating the merging of the two droplets at impact. Eqs. (1) and (3) are then reformulated to:

$$\begin{aligned}\alpha_1 &= \frac{\text{Volume of droplet1}}{\text{Total volume of the control volume}}\\ \alpha_2 &= \frac{\text{Volume of droplet2}}{\text{Total volume of the control volume}}\end{aligned} \tag{6}$$

The values of density and viscosity are calculated as a function of "α", using linear interpolation between the values of the two phases:

$$\begin{aligned}\rho &= (\alpha_1 + \alpha_2)\rho_{liq} + (1 - \alpha_1 - \alpha_2)\rho_{gas}\\ \mu &= (\alpha_1 + \alpha_2)\mu_{liq} + (1 - \alpha_1 - \alpha_2)\mu_{gas},\end{aligned} \tag{7}$$

where the "α"-function is equal to:

$$a_1(x,t) = \begin{cases} 1, & \text{for a point } (x,t) \text{ inside liquid (droplet1)} \\ 0, & \text{for a point } (x,t) \text{ outside liquid} \\ 0 < \alpha_1 < 1, & \text{for a point } (x,t) \text{ inside gas} \\ & \text{transitional area between the two phases} \end{cases}$$

$$a_2(x,t) = \begin{cases} 1, & \text{for a point } (x,t) \text{ inside liquid (droplet2)} \\ 0, & \text{for a point } (x,t) \text{ inside gas} \\ 0 < \alpha_2 < 1, & \text{for a point } (x,t) \text{ inside the} \\ & \text{transitional area between the two phases} \end{cases}$$

$$a_1(x,t) + a_2(x,t) = \begin{cases} 1, & \text{for a point } (x,t) \text{ inside liquid (coalesced droplet)} \\ 0, & \text{for a point } (x,t) \text{ inside gas} \\ 0 < \alpha < 1, & \text{for a point } (x,t) \text{ inside the} \\ & \text{transitional area between the two phases} \end{cases} \tag{8}$$

The conservative form of each transport equation for the indicator function "α_i"$_{=1,2}$ is written as:

$$\frac{\partial a_i}{\partial t} + \nabla \cdot a_i \vec{u} = 0, \quad i = 1, 2 \tag{9}$$

'As it was mentioned in the introduction, a thin gas layer is formed between the two approaching droplets. When the thickness of the gas layer becomes comparable to the intermolecular spacing (about 100–400 Å) the liquid surface ruptures and the approaching droplets coalesce (Mackay and Mason [12] and Bradley and Stow [13]). Even using the present technique of local grid refinement, such a small length scale cannot be resolved. In the present investigation the layer ruptures (numerically) at a prescribed time, according to the corresponding experimental data, by simply removing the double interface between the two droplets, leaving a single droplet with an indented waist (Nobari et al. [23]). This instantaneous change in topology is a gross approximation because the influence of molecular forces and the small isolated droplets that may be formed during the rupture are not modeled. Furthermore, as the interface is ruptured the total volume and kinetic energy of the liquid phase are not altered. However, there is a reduction in surface energy due to the elimination of the common surface between the two droplets; this energy is supposed to be lost when the ruptured film breaks into small droplets which are finally dissipated.

2.3. The numerical solution procedure

The transport equations are solved numerically by the Finite Volume Method using a collocated grid arrangement. The discretization of the convection terms of the velocity components is based on a high-resolution convection-diffusion differencing scheme (Gamma scheme) proposed by Jasak [35],. The solution procedure for the momentum and continuity equations is based on the SIMPLE algorithm of Patankar and Spalding [36] with the modifications of Rhie and Chow [37] to avoid pressure–velocity decoupling. Due to the steep gradients of the V.O.F indicator function "α" which appear particularly in the region of the interfaces, it was found necessary to implement the compressive high-resolution differencing scheme CICSAM proposed by Ubbink and Issa [38]. In contrast with other discretization schemes, which fail to capture the sharp but smooth interface transition between the two fluids, the CICSAM scheme limits the transitional area of the two fluids within two cells and achieves good resolution of the transitional region. The time derivative was discretized using a second-order differencing scheme (Crank–Nicolson). A demonstration of the non-diffusive character of the CICSAM scheme can be found in Theodorakakos and Bergeles [33].

2.4. Numerical details

The main parameters of the central binary collision process are the droplet diameter D_o the initial impact velocity U_o, the density ρ and viscosity μ of the liquid and gas as well as the surface tension σ. These variables are grouped in two dimensionless parameters, the Weber (We) and Reynolds numbers (Re) defined as:

$$We = \partial_{liq}(2U_0)^2 D_0 / \sigma \tag{10}$$
$$Re = \partial_{liq} 2U_0 D_0 / \mu_{liq} \tag{11}$$

In order to implement computationally the collision process, there are two alternatives:

(a) The droplets start suddenly with the collision velocities, defined by the corresponding Weber number and are placed at a small distance, at time $t = 0$. The corresponding gas velocity field at time $t = 0$. is assumed to be zero. The continuity and momentum equations are solved both for the gas and liquid phases at each time step (very small time step, 10^{-06} s). Therefore, at each time step both continuity and momentum equations are satisfied and after three to four time steps the induced gas and liquid velocity fields around the moving droplets are fully developed, well before collision takes place.

(b) The droplets have initially zero velocities and are separated by a long distance. An adjustable force is then used to drive the two droplets closer and is turned off shortly before the impact takes place after the collision velocities have been achieved (Nobari et al. [23,24]).

In the present study alternative (a) was chosen in order to reduce the computer time, with collision velocity satisfying the value of the Reynolds number of the numerical simulation of Nobari et al. [23] and Nobari and Tryggvason [24] or of the experimental data of Qian and Law [11].

The computational domain is shown in Fig. 1. The solution domain is axi-symmetric (around the X axis), and the droplets are initially placed one diameter apart. Both droplets have the same velocity U_o, and diameter D_o. At $Y = 0$, symmetry boundary conditions are imposed, whilst for the other boundaries the normal gradient is equal to 0. The experimental investigation of equally-sized droplets of Qian and Law [11] forms the basis of the present numerical simulation.

Table 1 summarizes the cases investigated. In cases A–D the liquid phase is n-tetradecane and the gas phase is nitrogen at atmospheric pressure. Cases A to C have been studied experimentally by Qian and Law [11]. The droplet collision was assumed to be isothermal at $T = 21\ °C$. In the experiments for cases A, B and C the collision was not ideally central as it is indicated by the small values of the impact parameter B (defined as $B = X/D_0$, where X is the lateral distance between the centers of the two droplets in a direction normal to the velocity).

For cases A to D, the "base" grid consisted of 1800 numerical cells, as shown in Fig. 1, covering a rectangular domain with dimensions $X_{tot} = 6.5\ D_o$, $Y_{tot} = 3.25\ D_o$ approximately. Five levels of local grid refinement are used, resulting to a maximum number of 10,500 cells for cases A and B, 22,000 for case C and 32,000 for case D. The maximum refinement results in a cell size of $D_o/300$. Obviously, computations are more time efficient on the present dynamically adaptive grid, than on the equivalent fine resolution and uniform grid. Cases A, B, C and D would require approximately 1,845,120 number of cells in a uniform fine grid.
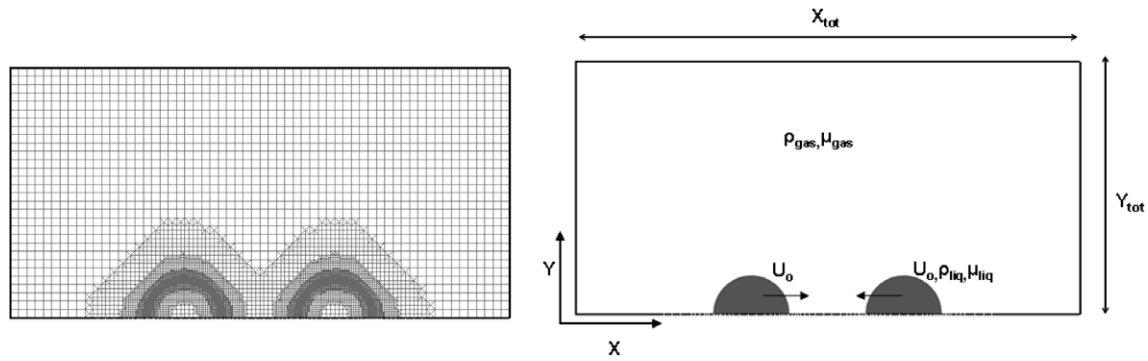
Fig. 1. The computational domain and the base grid with the five levels of local grid refinement around the interface.

Table 1
Cases examined.

Case	We	Re	Ro = Do/2 (m)	B (experimental)	Computational domain ($X_{tot} \times Y_{tot}$)	Number of grid nodes
A	8.6	105.9	1.53E-04	0.08	13.07Ro × 6.53Ro	60 × 30 (5 levels-local refinement)
B	19.4	158	1.51E-04	0.05	13.24Ro × 6.62Ro	60 × 30 (5 levels-local refinement)
C	61.4	296.5	1.68E-04	0.06	11.90Ro × 5.95Ro	60 × 30 (5 levels-local refinement)
D	123	423.76	1.68E-04	–	17.85Ro × 5.95Ro	60 × 30 (5 levels-local refinement)
E	61.4	24.5	1.68E-04	–	14.8Ro × 5.95Ro	126 × 50 (3 levels-local refinement)
F	61.4	29	1.68E-04	–	14.8Ro × 5.95Ro	127 × 50 (3 levels-local refinement)
G	61.4	33	1.68E-04	–	14.8Ro × 5.95Ro	128 × 50 (3 levels-local refinement)
H	61.4	70	1.68E-04	–	14.8Ro × 5.95Ro	129 × 50 (3 levels-local refinement)
I	61.4	131	1.68E-04	–	14.8Ro × 5.95Ro	130 × 50 (3 levels-local refinement)
J	61.4	228	1.68E-04	–	14.8Ro × 5.95Ro	131 × 50 (3 levels-local refinement)
K	61.4	404	1.68E-04	–	14.8Ro × 5.95Ro	132 × 50 (3 levels-local refinement)
L	61.4	498	1.68E-04	–	14.8Ro × 5.95Ro	133 × 50 (3 levels-local refinement)
M	61.4	903	1.68E-04	–	14.8Ro × 5.95Ro	134 × 50 (3 levels-local refinement)
N	61.4	1790	1.68E-04	–	14.8Ro × 5.95Ro	135 × 50 (3 levels-local refinement)
O	61.4	3570	1.68E-04	–	14.8Ro × 5.95Ro	136 × 50 (3 levels-local refinement)
P	61.4	7653	1.68E-04	–	14.8Ro × 5.95Ro	137 × 50 (3 levels-local refinement)
Q	61.4	11538	1.68E-04	–	14.8Ro × 5.95Ro	138 × 50 (3 levels-local refinement)

In order to investigate the grid dependency of the results, cases A and B were also simulated using six levels of local refinement, resulting in a minimum cell size equal to $D_o/600$. The numerical results indicated that using five levels of local grid refinement for case A, the hydrodynamic behaviour of the impacting droplets did not change, with the magnitude of total velocity change being only approximately 0.7% and the collision development to be almost identical to that of the coarser grid. However the liquid and gas velocities in the area between the two colliding droplets had a difference of 40% (mainly due to the fact that the size of this region tends to zero) but soon these differences were smoothed out. The numerical simulations take around 2 days on a Pentium 4 with a 2.4 GHz processor.

Further to that, case Q (highest Reynold number) was run for three and four levels of local refinement resulting in cell sizes $D_o/135$ and $D_o/270$, respectively. The results were almost identical, showing difference in droplet's dimensions of less than 1%.

3. Collision of two droplets of equal sizes

3.1. Bouncing of two equal-sized droplets, case A, low We number impact

As discussed earlier, coalescence can not occur when the droplets approach each other unless the gaseous film is 'squeezed out' and then contact is made. Clearly, the 'discharging' of the gaseous layer, depends on the inertia of the droplets and the dynamics of the flow including the pressure buildup within it. After completing a wide range of experiments for tetradecane droplets in nitrogen

environment under atmospheric pressure, Qian and Law [11], determined that for head-on collisions (B = 0) the critical We number, above which coalescence occurs, is around We = 14.3.

As the We number of case A (see Table 1) is below this critical We number, the two droplets are expected to bounce off without coalescence. Fig. 2a shows a sequence of photographs from the experiments of Qian and Law [11] and the present simulations. The deformation and the shape of the two colliding droplets at various time instants after contact are in very good agreement. In this case no coalescence occurs, the two droplets retain their identity during the collision process and a gas layer always exists between them. In Fig. 2b the intervening gas layer between the two droplets is clearly shown ($t = 0.20$) as it has been also found by Mackay and Mason [12]. This layer remains there until the end of the receding phase of the colliding droplets ($t > 0.91$). The width of the gas layer is equal to 4.164 μm and it is resolved by at least three cells. According to Qian and Law [11] the gap between the droplets is estimated to be of the order of $(\rho_g R_o^3 U_o^2/\sigma)^{1/2}$ which gives a value of 6.146 μm, in rough agreement with the aforementioned value. It is interesting to note that there is always a cusp in the contact region that indicates that the two droplets have not coalesced yet.

As the two droplets approach each other, pressure in the air gap increases, the liquid surfaces deform and flatten while gas is squeezed out creating a sheet jet (Fig. 3, $t = 0.10$ ms). Surrounding gas is entrained into this jet and on either side of the jet a vortex ring is formed. These vortex rings remain close to the liquid surface during the collision process. The strength of the vortices attains a minimum value at the time of maximum deformation ($t = 0.43$ ms), and a maximum value at the first stages of the collision. The vortices change rotational direction during the receding phase, as gas
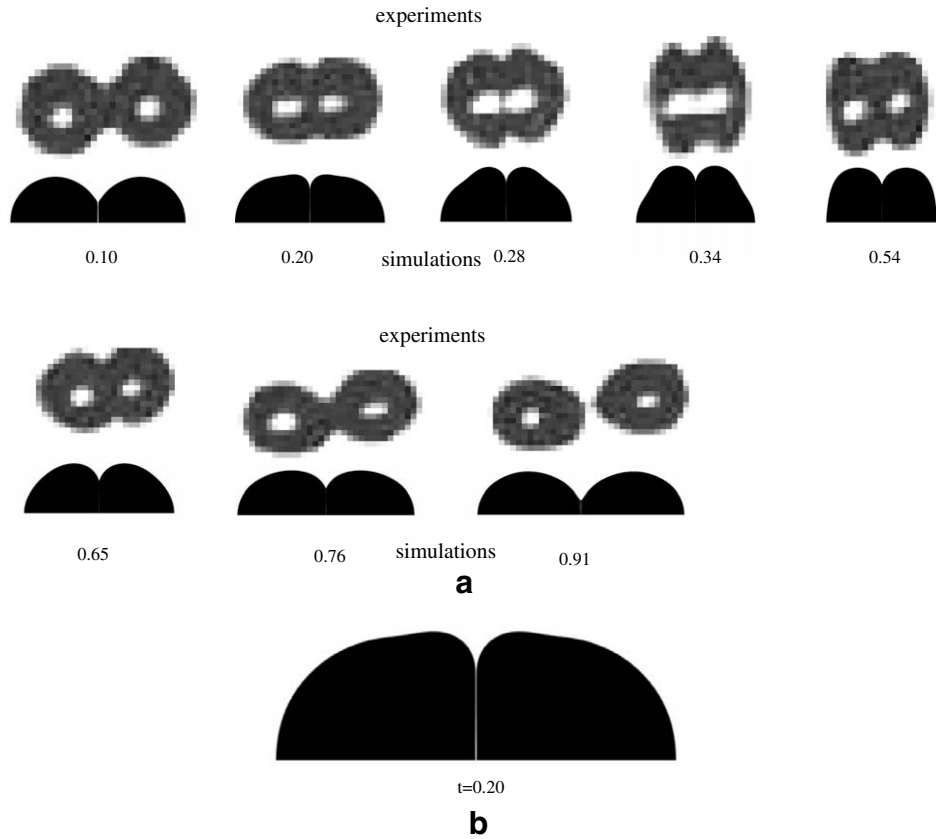
Fig. 2. (a) Time evolution for two colliding droplets, Case A (We = 8.6, Re = 105.9) and (b) gas film entrapment between the two approaching droplets; experiment of Qian and Law.
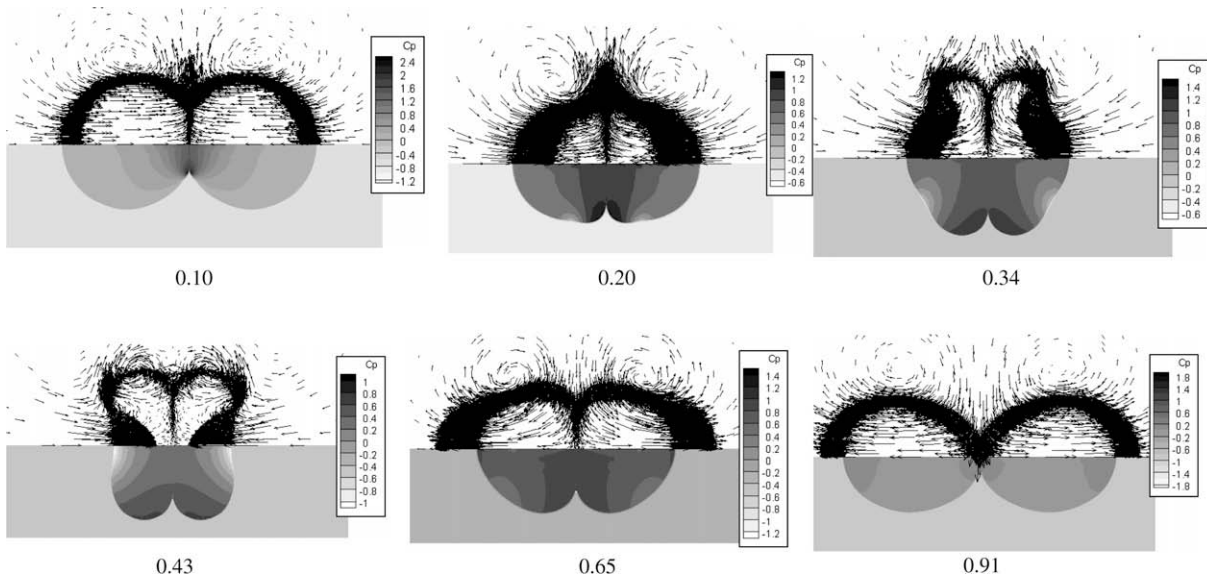

Fig. 3. Pressure and velocity field evolution for Case A (We = 8.6, Re = 105.9).

accelerates to fill in the gap between the two separating droplets ($t > 0.43$ ms).

It is interesting to notice the continuity of the velocity field through the gas–liquid interface, as well as the well-defined interface, an indication of the non-diffusive character of the CICSAM discretization scheme of Ubbink and Issa [38]. The maximum gas jet and liquid jet velocities are 656% and 154%, respectively, of

the droplet's impact velocity. Fig. 3 also shows the distribution of the pressure coefficient C_p within the droplets during collision. C_p is based on the relative velocity of droplets i.e., $C_p = \Delta P/(0.5\ \rho_{liq}\ (2U_o)^2)$. Values of C_p up to 442% at the front stagnation point are developed with the maximum pressure developing at the periphery of the droplet–film contact area. Pressure builds up very fast, and then decreases with time (Fig. 3).

3.2. Coalescence of two droplets, case B, medium We number impact

In case B experiments suggest that coalescence of the two colliding droplets should take place due to the higher Weber number compared with case A. According to Qian and Law [11] the cusp at the rim of the droplets in the gap area disappears at the moment of coalescence and a rounded profile is established. Based on this observation the experiments suggest that coalescence takes place between $t = 0.31$ ms and $t = 0.35$ ms. In the present simulation the prescribed time of coalescence is fixed to 0.31 ms. The predicted deformation and shape of the two colliding droplets at various time instants after contact is compared with experiments in Fig. 4. It can be seen that the overall time evolution of the droplet's shape is well captured.

As in the previous case, a sheet of gas jet between the two approaching droplets is formed. On either side of the jet, one vortex ring is formed, whose strength is higher compared to the previous case A (Fig. 5, $t = 0.08$ ms). The maximum gas and liquid jet velocities are 700% and 183%, respectively, of the droplet's impact relative velocity. The maximum pressure coefficient is 321% and is found at the periphery of the droplets contact area. In addition, just after coalescence, a nitrogen gas bubble is entrapped inside the coalesced droplet. At time $t = 0.33$ ms, its volume is equal to 0.0845% of the initial volume of both droplets. The coalesced droplet mass oscillates before it equilibrates. The kinetic energy is partly dissipated into the internal motion within the droplet and, as it will be shown later to a much smaller extent, in the gas flow inside the gap.

3.3. Coalescence of two droplets, case C, high We number impact

In case C coalescence occurs just as in the previous case B, because the kinetic energy of the droplets seems to be high enough to 'squeeze out' the intermediate air film between them. The difference between the two cases is that now the two droplets coalesce almost immediately after their initial contact. Another characteristic of the present case is that coalescence of the two initial droplets is followed by separation, indicating that the present Weber number of 61.4 is above the critical number separating the regions of coalescence and separation. After coalescence, the merged droplets continue to deform in such a way as to form a boundary ring with a thin connecting liquid disc inside (Fig. 6, $t = 0.45$ ms). At $t = 0.6$ ms,

most of the liquid mass has been accumulated in the boundary ring and a hole is created at the center of the thin disc. After $t = 0.6$ ms, the radial velocity reverses its direction towards the center of the disc, the central hole fills up and the ring shape is gradually transformed to a bell shape, extending in length in the axial direction in agreement with the experiments (Fig. 6, $t = 0.85$ ms and $t = 1.2$ ms). Due to the outward liquid motion along the axis of symmetry, a ligament connecting the two boundary droplets is formed and its length is increasing with time (Fig. 6, $t = 1.95$ ms). The tip droplets grow in size and the ligament becomes thinner up to $t = 2.2$ ms (around $t = 2.0$ ms according to experiments) when it is cut off from the boundary droplets. Subsequently surface tension effects transform the ligament to a satellite droplet (Fig. 6, $t = 2.50$ ms) in agreement with the experimental data of Qian and Law [11].

The velocity and pressure field at various time instants is shown in Fig. 7. The value of the maximum gas and liquid jet velocities is 1041% and 457% of the droplet's impact velocity, respectively. The maximum pressure developed is 407%. Air bubbles are also trapped within the liquid phase but their volume is equal to 0.02% of the initial volume of both droplets (Fig. 6, $t = 0.05$ ms), less than in the previous case. Each of the two main droplets has a volume of 49.36% of the initial total volume while the small satellite droplet has a volume of 1.27% of the total. The diameters are 99.57% D_o and 29.4% D_o, respectively.

3.4. Coalescence and separation of two droplets, case D, higher We number impact

Experimental results for this case don't exist. Just like case C the two droplets coalesce at once after their contact, forming a shape like 'donut' at the time of maximum deformation (Fig. 8, $t = 0.38$ ms). Subsequently, the coalesced droplet recedes towards the symmetry axis and elongates along it, forming a cylindrical ligament between the two boundary droplets. Due to the same mechanism as in case C, the merged droplet separates in two end droplets and one central satellite droplet at $t = 2.90$ ms. The difference between case C and D is the extent of ligament's deformation. In the present case, the length of the ligament just before it pinches off from the boundary droplets is bigger and equal to 6.76 R_o at $t = 2.06$ ms, compared to 2.07 R_o at $t = 2.16$ ms for case C. Also the size of the central satellite droplet is comparable to the size of the two end main droplets, whilst in
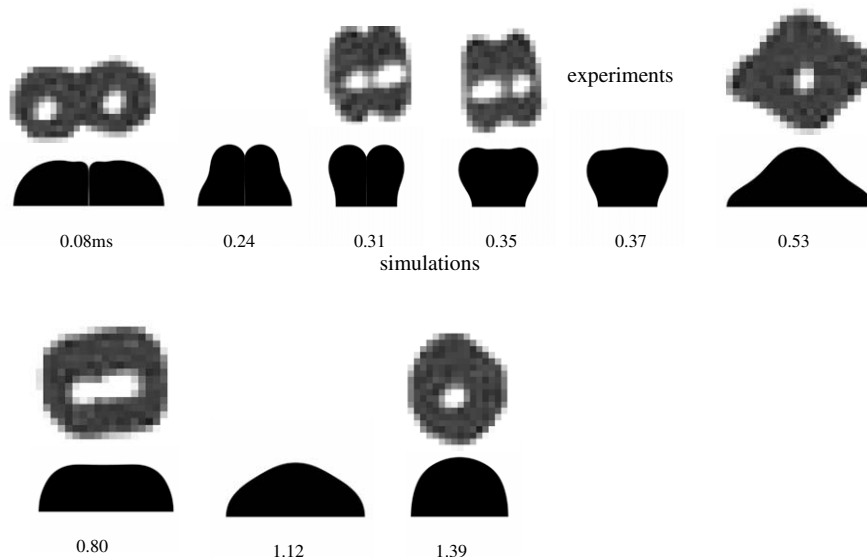

Fig. 4. Time evolution of two colliding droplets for Case B (We = 19.4, Re = 158); experiment of Qian and Law.
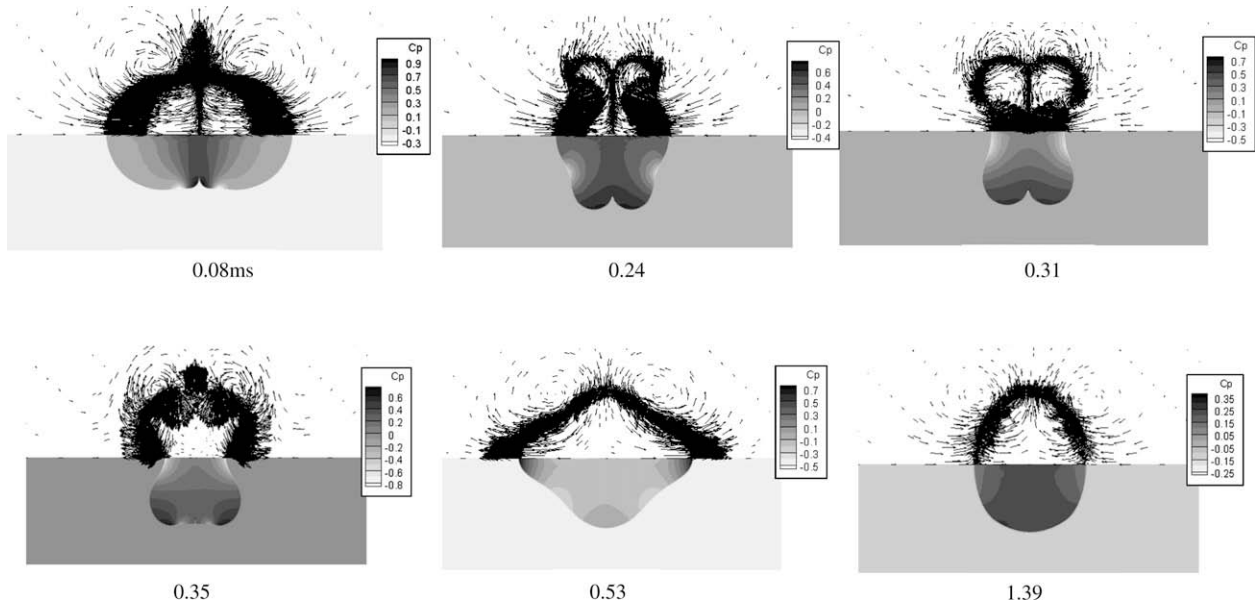
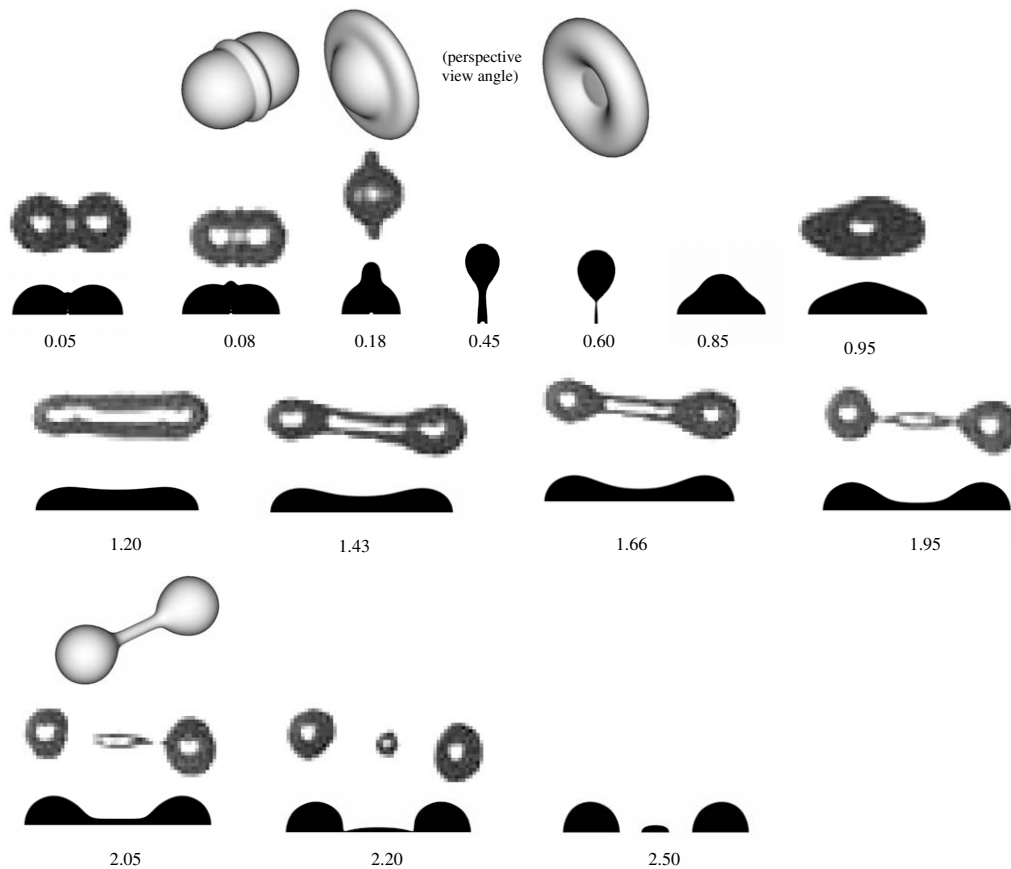**Fig. 5.** Pressure and velocity field evolution for Case B (We = 19.4, Re = 158).

Fig. 6. Time evolution of collision for Case C (We = 61.4, Re = 296.5); experiment of Qian and Law.

case C it was much smaller. Each of the two end droplets has a volume of around 31.2% of the initial total volume of the two droplets. The satellite droplet has a volume of around 37.6% of the initial total volume. The corresponding diameters are 85.46 D_o and 90.94% D_o, respectively.

The velocity and pressure fields are shown in Fig. 9. The value of the maximum gas and liquid jet velocities is around 1011% and

478% of the droplet's impact relative velocity, respectively. The maximum pressure developed is 299. The values of maximum non-dimensional gas and liquid velocities in cases C and D are almost equal, indicating the similarity of the coalescence process after impact, for high Weber number impacts. The volume of the air bubble entrapped is equal to 0.016% of the initial volume of both droplets.
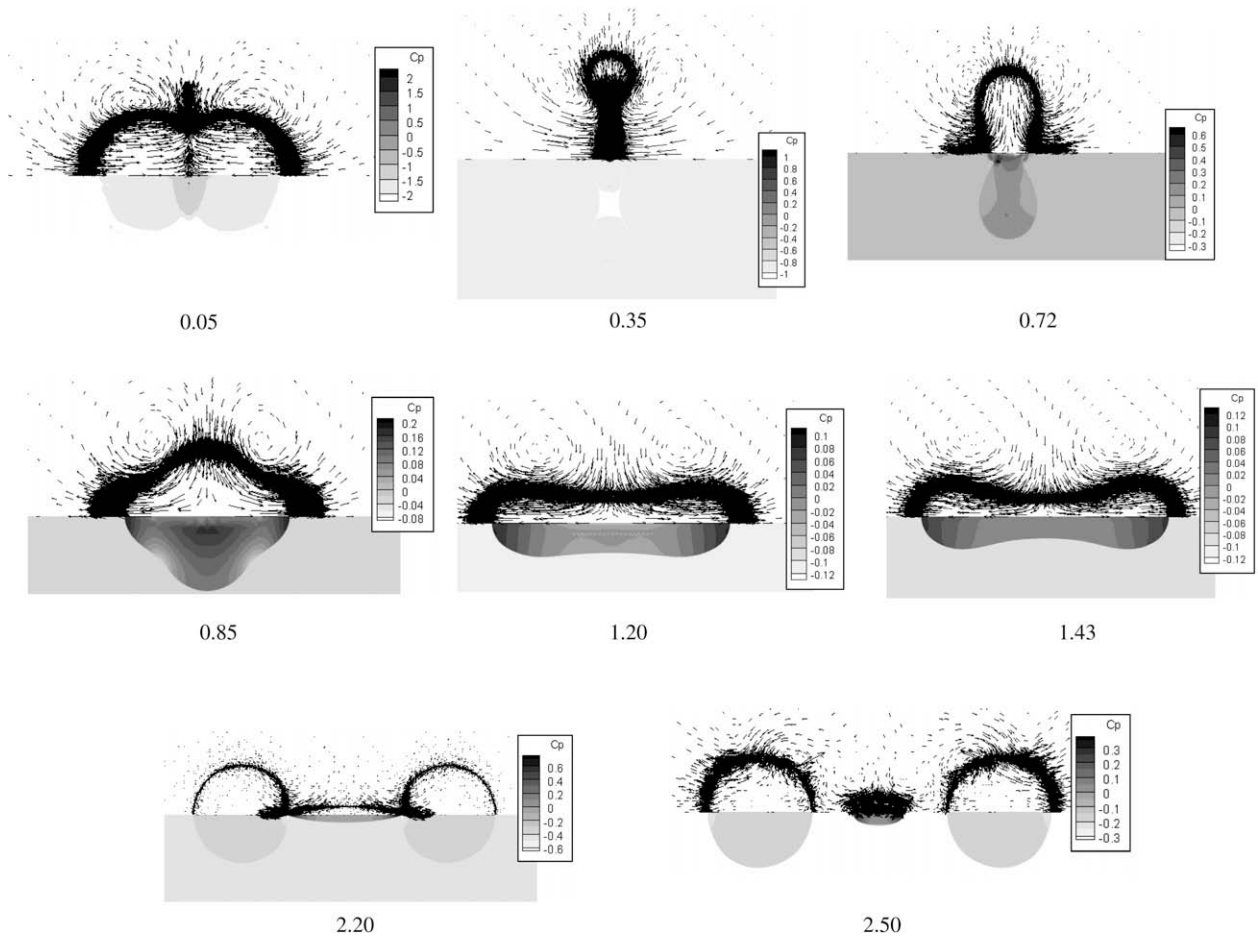
0.05   0.35   0.72

0.85   1.20   1.43

2.20   2.50

Fig. 7. Pressure and velocity field evolution for Case C (We = 61.4, Re = 296.5).

0.06ms   0.22   0.38   0.85   1.06   2.04
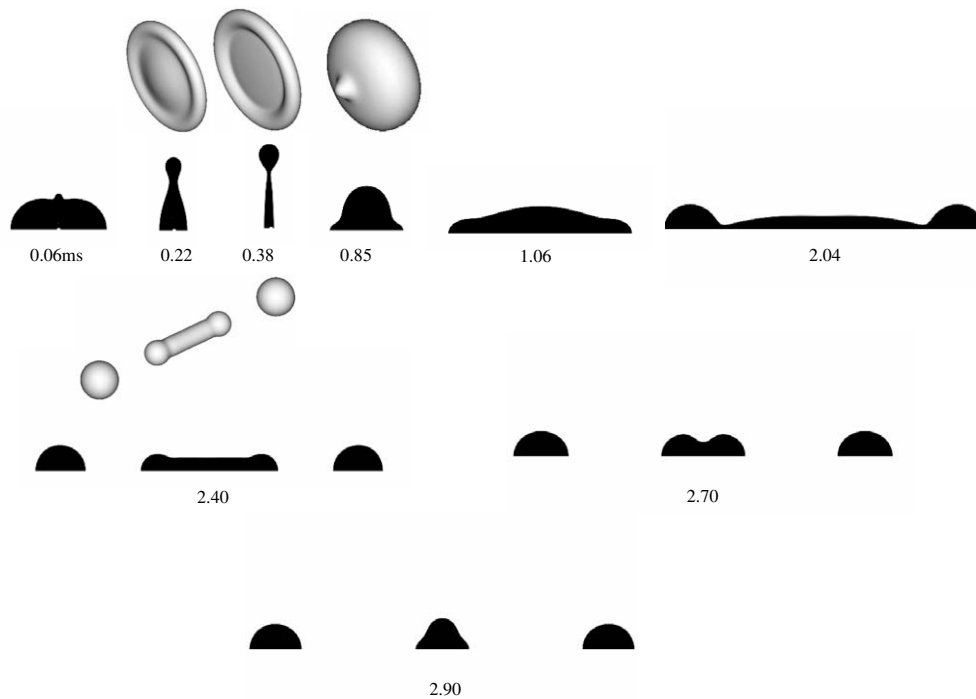
2.40   2.70

2.90

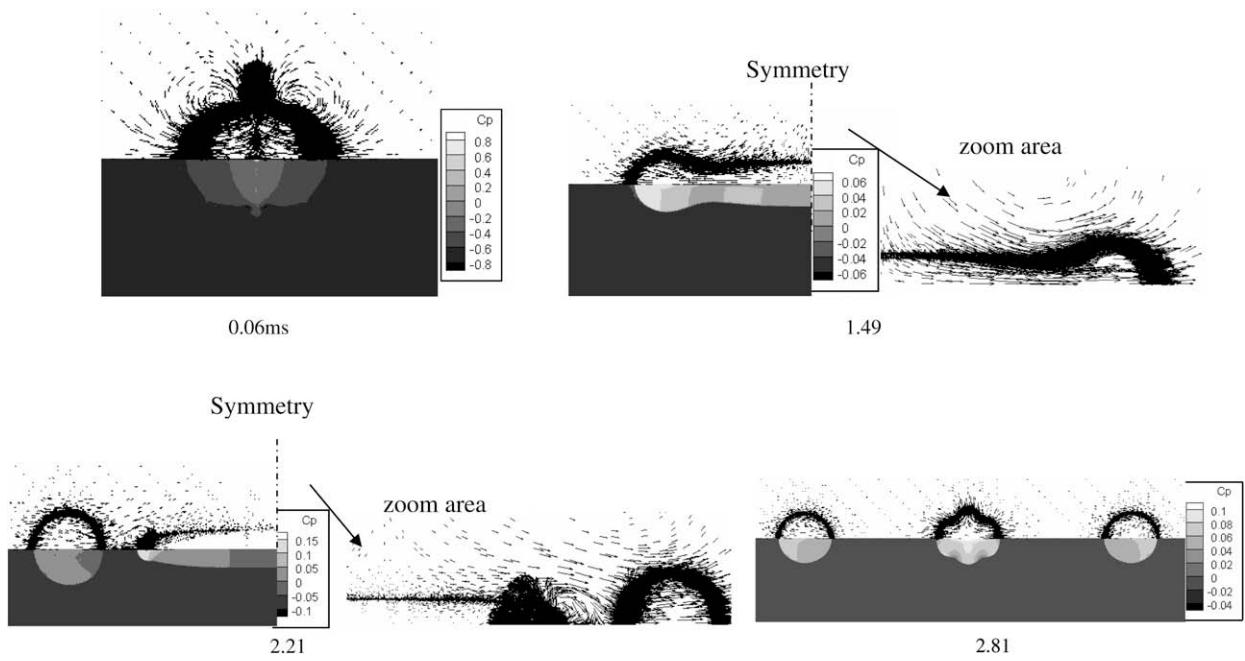**Fig. 8.** Time evolution for Case D (We = 122.8, Re = 423.76).

Fig. 9. Pressure and velocity field evolution for Case D (We = 122.8, Re = 423.76).
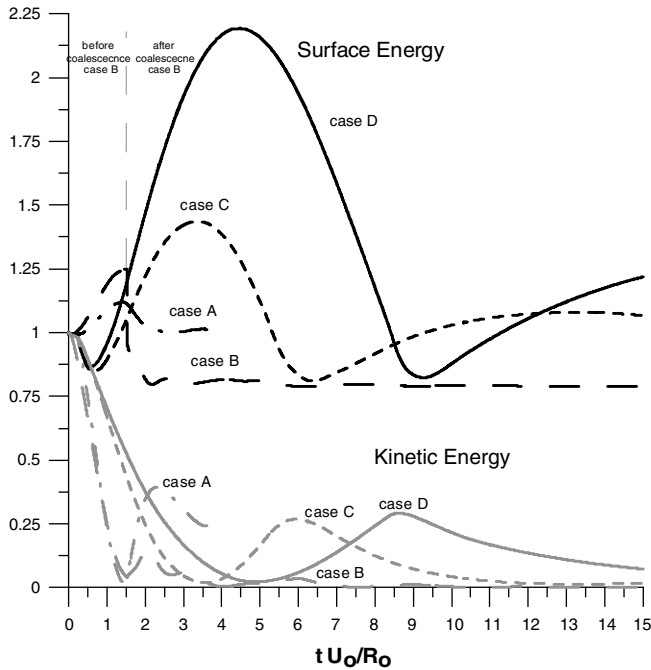

Fig. 10. Surface and kinetic energy of colliding droplets with time for cases A, B, C and D.

4. Characteristics of the flow field

4.1. Time evolution of surface and kinetic energy of droplets

Fig. 10 shows the evolution of kinetic (E_k) and surface (E_s) energies of the colliding droplets as a function of time. E_k is defined as $\Sigma[0.5\rho_{liq}(\alpha V_{cell})(2U_0)^2]$ where the summation is taken over the whole computational domain and $E_s = \sigma$ (Area), where (Area) is the surface of the liquid phase. Before coalescence the total surface of the colliding droplets is taken into account in the surface energy calculations. After coalescence only the external surface of the

merged droplet is considered; therefore coalescence is indicated by the discontinuous change of the surface energy.

In cases A and B (for which the ratio of the initial surface energy to kinetic is 5.74 and 2.54, respectively, i.e., larger than one) during the approaching phase, the surface energy of the two droplets increases whilst the kinetic energy decreases, both obtaining maximum and minimum values, respectively, at the time of maximum droplet deformation. Then for case A the kinetic energy recovers at the expense of surface energy while for case B it is almost lost on coalescence. In case B upon coalescence, there is a loss of surface energy; afterwards it tends to be stabilised at 80% of the initial surface energy while the kinetic energy approaches zero value. In cases C and D (for which the ratio of the initial surface energy to kinetic is 0.803 and 0.401, respectively, i.e., lower than one), upon droplet contact, there is an almost immediate coalescence with a small loss of surface energy. After coalescence the surface energy increases at the expense of the kinetic energy and then after reaching its maximum value, it tends to a constant value around unity in an oscillatory way, whilst the corresponding values of the kinetic energy tend to zero, indicating that the kinetic energy is lost.

According to Jiang et al. [10] the maximum droplet deformation S_{max} is independent of the energy dissipation, (expressed by the loss coefficient "a") and of the Reynolds number and depends only on Weber number, as shown in Eq. (12)

$$\frac{S_{max}}{S_o} = 1 + (1 - a) \cdot We/48 \qquad (12)$$

where S_o the initial surface and "a" = 0.5.

This conclusion contradicts recent results by Willis et al. [18] and Dai and Schmidt [19], which indicate that the loss coefficient "a" is Reynolds dependent. In order to resolve this contradiction, a parametric study was carried out as shown by cases E, F, G to Q in Table 1, keeping the Weber number constant and changing the Reynolds number. Fig. 11 presents the dimensionless viscous dissipation rate $(\theta\Phi/\theta t)/(\pi\rho_{liq}R_o^2U_o^3)$ as a function of the dimensionless time t/T_1 both in the gas and liquid phases, where Φ is the dissipated energy as defined by Dai and Schmidt [19]. The results shown in Fig. 11a indicate that for the same Weber number the loss of kinetic energy takes place mainly in the liquid phase
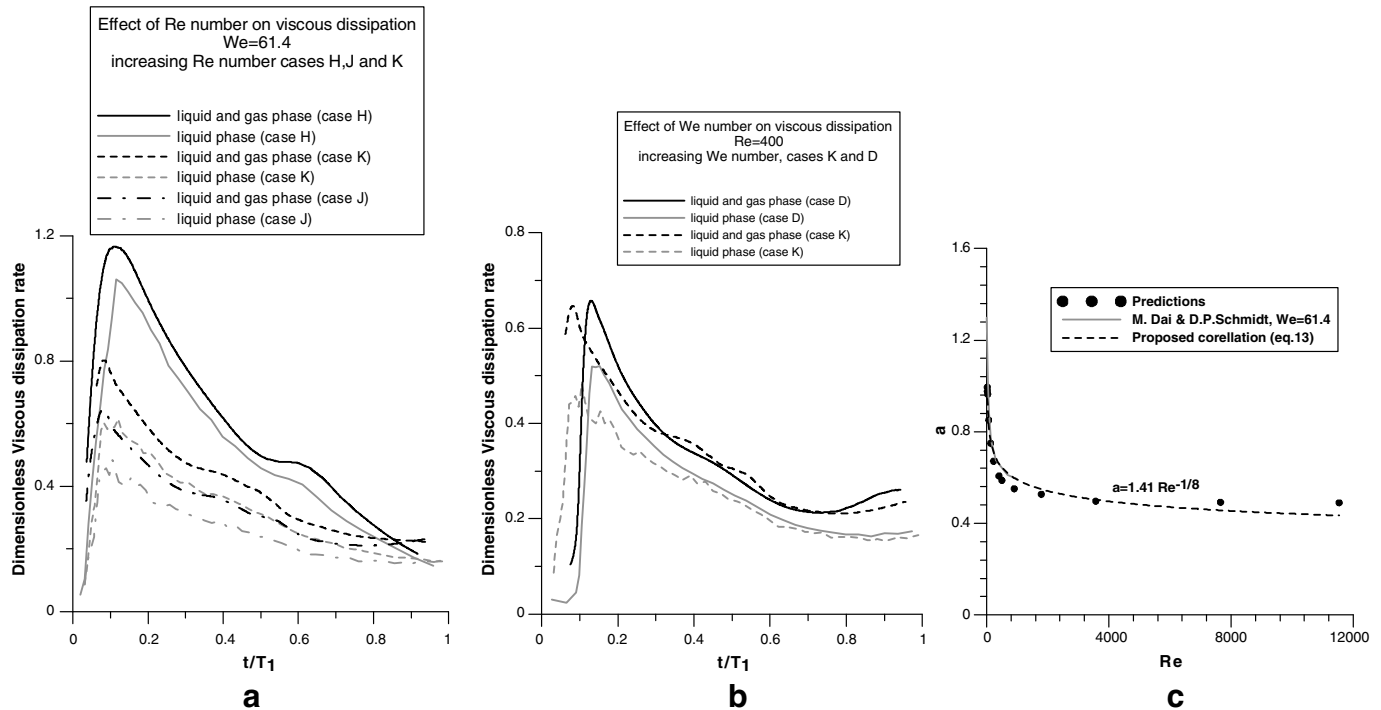
Fig. 11. Effect of We and Re numbers on viscous dissipation.

and the small part that it is lost in the gas phase increases with the Reynolds number. Fig. 11b shows the effect of the Weber number on the energy dissipation with almost constant Reynolds number. It can be seen that the energy lost in the gas phase is decreasing with the increase of the Weber number. It is interesting to notice that the dissipated energy takes place within one non-dimensional time ($T_1 = 2R_o/U_o$), as well as most of the loss of the kinetic energy.

Assuming that the loss coefficient "a" is Reynolds number dependent and using the results of the simulated cases E to Q of Table 1, a relation of the maximum deformation with Reynolds number can be found, shown in Fig. 11c. The loss coefficient "a" can be calculated from a best fit curve and the following relation is proposed (valid for We = 61.4).

$$a = 1.41^* \mathrm{Re}^{-1/8} \tag{13}$$

Eq. (13) shows that the loss coefficient "a" decreases with increasing Reynolds number and its influence diminishes at large Reynolds numbers, indicating that Jiang's [10] conclusion that the energy dissipation in period T_1 is independent of Reynolds number (or viscosity) is indeed valid for high Reynolds numbers.

4.2. Mechanism of ligament breakup and satellite droplet formation

Just before ligament pinch off and satellite droplet formation, the liquid has small velocity from the centre of the ligament towards its edges (Fig. 12a, t = 2.21 ms and Fig. 12b, t = 2.16 ms) and a local maximum of pressure is built-up. The pressure near the seat of the pinch off is maximum (Fig. 12c, t = 2.21 ms), equal to C_p = 0.8; towards the boundary droplet the pressure gradient is very high and the liquid velocity which is very small and negative (defined as positive if directed towards the centre of impact and as negative in the opposite direction) increases in magnitude and becomes equal to $-0.8U_0$. This results in pumping liquid into the boundary droplets (Fig. 12a, t = 2.21 ms) thinning the ligament and creating a neck at the position of maximum velocity of high curvature. It is of importance to notice from Fig. 12a and c, that the two maxima of pressure and velocity are found at different

locations. At the moment of ligament pinch off (Fig. 12a, t = 2.22 ms), the liquid velocity draining the neck area is very high (almost $-2U_0$), whilst the almost zero velocity towards the location of maximum pressure existing at about time t = 2.21 ms, reverses sign (becomes positive) and is now directed towards the central part of the ligament. This contributes to both the ligament detachment and its subsequent shrinkage as well as to the further increase of the maximum pressure in the area, the location of which is shifted to the central part of the ligament ($C_p = 1$)(t = 2.23 ms). After detachment of the ligament from the boundary droplet, the velocity towards the ligament center increases substantially as shown in Fig. 12a (t = 2.23 ms) as well as the pressure, Fig. 12c, t = 2.23 ms. The shrinkage of the ligament continues until the formation of the satellite droplet.

Fig. 13 indicates the linear dimensions of the ligament in the axial (length) and radial (width) directions with time. The length of the ligament for case C (lower We number) is smaller compared to case D (higher We number) and the same stands for the width. At the moment of pinch off, the non-dimensional length shown in Fig. 13a for case D is 3.5 times larger compared to case C. After pinch off, the length of the ligament is reducing at very fast rate, whilst at the same time the width is increasing, due to ligament shrinkage. The ligament diameter at pinch off is 2.5 times higher in case D compared to case C but the ratio of ligament length to diameter is for case C 70% of that of case D.

5. Conclusions

The flow field arising from the head-on binary droplet collision between equal-sized droplets was numerically studied using a finite volume technique incorporating the volume of fluid (V.O.F) methodology and an adaptive local grid refinement approach. A higher order discretization scheme was found to be necessary for the numerical solution of the transport equation for the V.O.F variable in order to accurately track the droplet–gas interface. Also the use of two V.O.F indicators allowed the prediction of the collision process up to coalescence time, that was specified by the
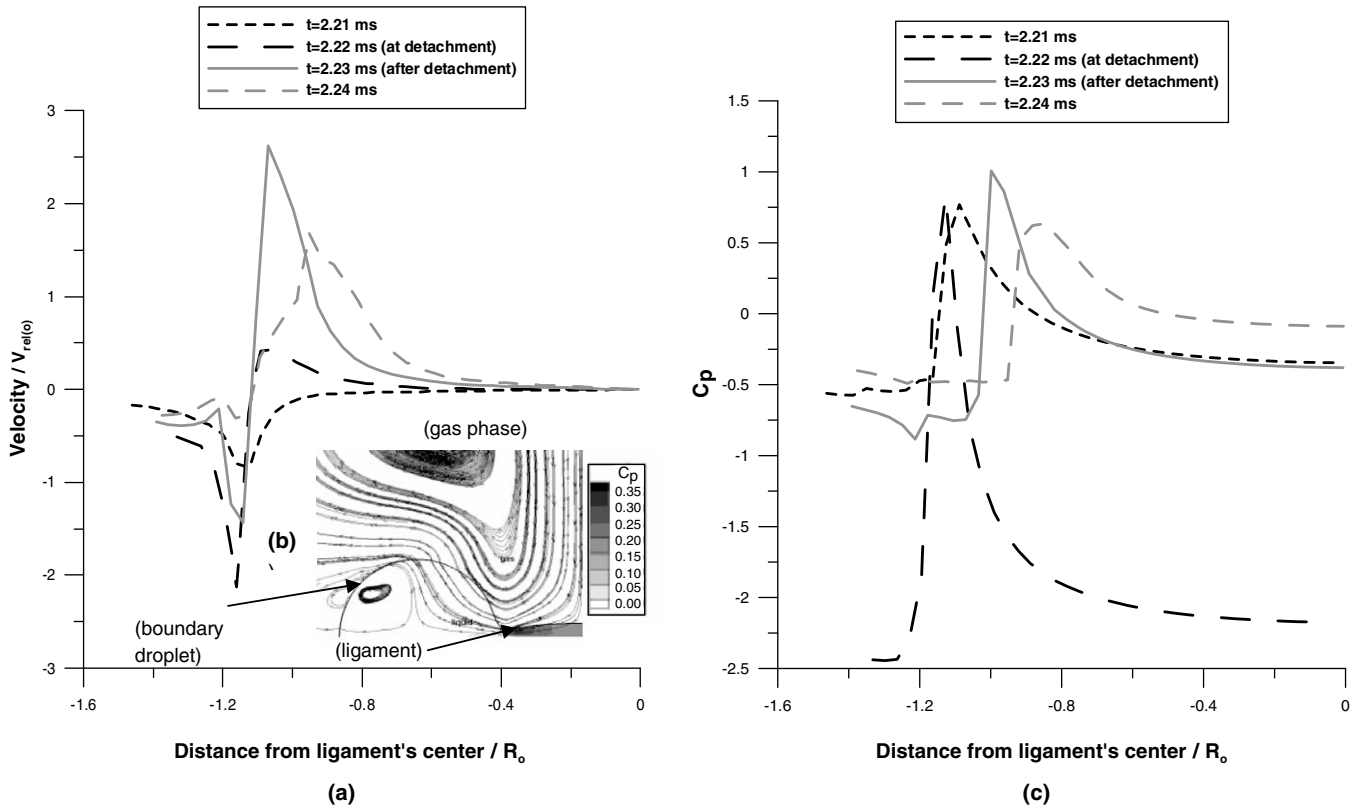
Fig. 12. Velocity and pressure distribution at the ligament detachment area for case C.
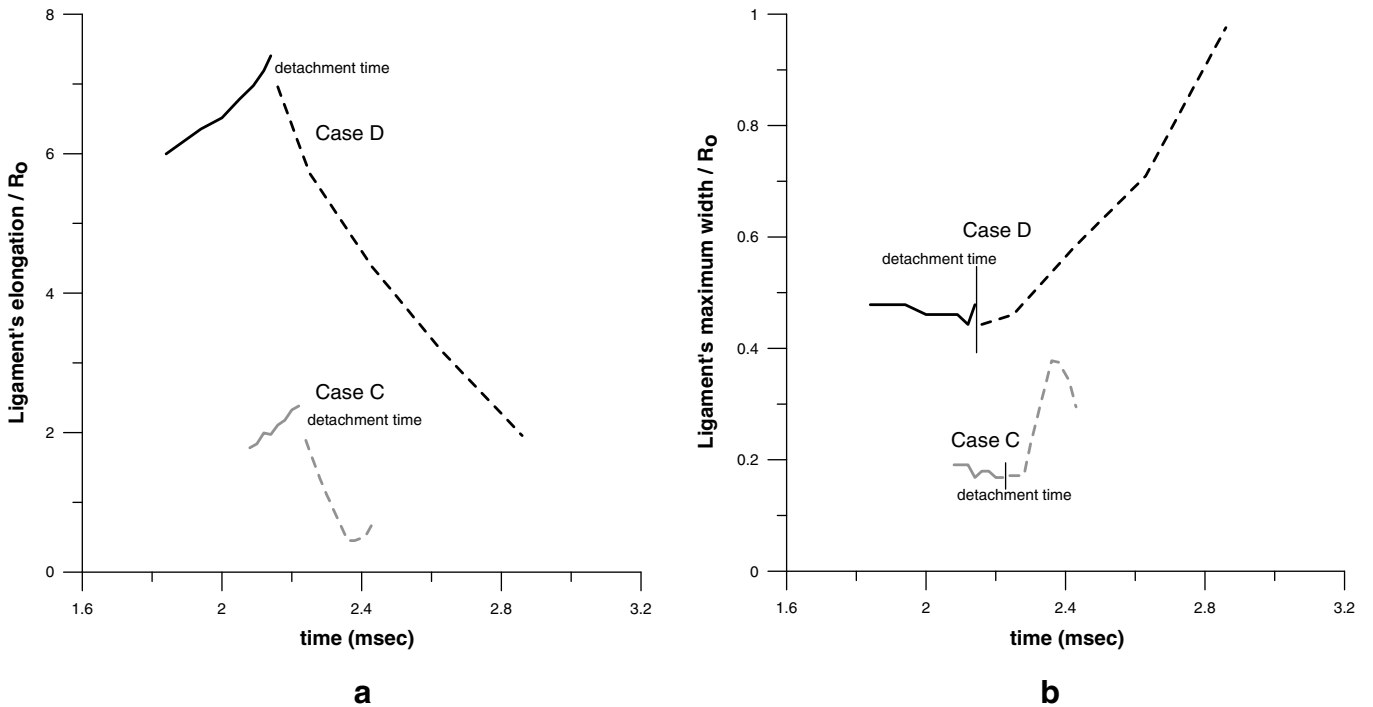

Fig. 13. Variations of the ligament's dimensions with time for cases C and D.

experimental data. The numerical results agree reasonably well with the corresponding experimental data. The V.O.F method was capable of predicting the details of the flow, like gas bubble entrapment, droplet deformation, gas and liquid jetting and satellite drop-

let formation. When stretching separation occurs, the size of the central satellite droplet increases with the Weber number. Ligament pinch off from the end droplets occurs due to the increased pressure at the ligaments ends and the associated flow drainage to-

wards to ligament's edges at first place and at subsequent times to ligament's central part (flow reversal). Initially droplet kinetic energy upon collision is transformed into surface energy while later the opposite occurs in an oscillatory way. Loss of energy due to viscous dissipation is mainly due to viscous losses within the liquid phase. The dissipation loss coefficient is Reynolds number dependent but this dependency becomes insignificant at large Reynolds numbers.

Acknowledgment

References

[1] Adam JR, Lindblad NR, Hendricks CD. The collision, coalescence, and disruption of water droplets. J Appl Phys 1968;39:173.
[2] Park RW. Behavior of water drops colliding in humid nitrogen. Ph.D. thesis, Department of Chemical Engineering, The University of Wisconsin; 1970.
[3] Brazier-Smith PR, Jennings SG, Latham J. The interaction of falling water drops: coalescence. Proc R Soc Lond A 1972;326:393.
[4] Ashgriz N, Poo JY. Coalescence and separation in binary collision of liquid drops. J Fluid Mech 1990;221:183–204.
[5] Ashgriz N, Givi P. Binary collision dynamics of fuel droplets. Int J Heat Fluid Flow 1987;8:205.
[6] Ashgriz N, Givi P. Coalescence efficiencies of fuel droplets in binary collisions. Int Commun Heat Mass Transfer 1989;16:11.
[7] Brenn G, Frohn A. Collision and merging of two equal droplets of propanol. Exp Fluids 1989;7:441.
[8] Brenn G, Frohn A. Collision and coalescence of droplets of various liquids. J Aerosol Sci 1989;20(8):1027–30.
[9] Willis KD, Orme ME. Experiments on the dynamics of droplet collisions in a vacuum. Exp Fluids 2000;29:347–58.
[10] Jiang YJ, Umemura A, Law CK. An experimental investigation on the collision behaviour of hydrocarbon droplets. J Fluid Mech 1992;234:171.
[11] Qian J, Law CK. Regimes of coalescence and separation in droplet collision. J Fluid Mech 1997;331:59.
[12] Mackay GD, Mason SG. The gravity effect approach and coalescence of fluid drops at liquid interfaces. Can J Chem Eng 1963;41:203.
[13] Bradley SG, Stow CD. Collision between liquid drops. Philos Trans R Soc Lond 1978;Ser. A287:635.
[14] Tsamopoulos JA, Brown RA. Nonlinear oscillations of inviscid drops and bubbles. J Fluid Mech 1983;127:519.
[15] Patzek TW, Benner RE, Basaran OA, Scriven LE. Nonlinear oscillation of inviscid free drops. J Comput Phys 1991;97:489.
[16] Foote GB. A numerical method for studying liquid drop behavior; simple oscillations. J Comput Phys 1973;11:507.
[17] Lundgren TS, Mansour NN. Oscillations of drops in zero gravity with weak viscous effects. J Fluid Mech 1988;194:479.
[18] Willis KD, Orme ME. Binary droplet collisions in a vacuum environment: an experimental investigation of the role of viscosity. Exp Fluids 2003;34:28–41.
[19] Dai M, Schmidt DP. Numerical simulation of head-on droplet collision: effect of viscosity on maximum deformation. Phys Fluids 2005;17:041701.
[20] Unverdi SO. Numerical simulation of multi-fluid flows. Ph.D. thesis, The University of Michigan; 1990.
[21] Unverdi SO, Tryggvason G. A front tracking method for viscous incompressible flows. J Comput Phys 1992;100:25.
[22] Unverdi SO, Tryggvason G. Computations of multi-fluid flows. Physica D 1992;60:70.
[23] Nobari MR, Jan Y-J, Tryggvason G. Head-on collision of drops – a numerical investigation. Phys Fluids 1996;8:29–42.
[24] Nobari MR, Tryggvason G. Numerical simulation of three dimensional droplet collision. AIAA J 1996;34(4):750–5.
[25] Lafaurie B, Nardone C, Scardovelli R, Zaleski S, Zanetti G. Modeling merging and fragmentation in multiphase flows with SURFER. J Comput Phys 1994;113:134.
[26] Drtina P, Schelkle M, Frohn A. Numerical simulation of droplet deformation and droplet coagulation applying lattice gas models. J Aerosol Sci 1991;22 (Suppl. 1):249–52.
[27] Schelkle M, Frohn A. Two dimensional lattice gas simulation of droplet deformation and non-central collisions. J Aerosol Sci 1993;26(Suppl. 1):S929–30.
[28] Schelkle M, Frohn A. Three-dimensional lattice gas simulation of binary collisions between equal droplets. J Aerosol Sci 1995;26(Suppl. 1):S145–6.
[29] Rieber M, Frohn A. Three-dimensional Navier–Stokes simulation of binary collisions between droplets of equal size. J Aerosol Sci 1995;24(Suppl. 1):513–5.
[30] Hirt CW, Nichols BD. Volume of fluid (VOF) method for the dynamics of free boundaries. J Comput Phys 1981;39:201–25.
[31] Nikolopoulos N, Theodorakakos A, Bergeles G. Normal impingement onto a wall film: a numerical investigation. Int J Heat Fluid Flow 2005;26:119–32.
[32] Brackbill JU, Kothe DB, Zemach C. A continuum method for modeling surface tension. J Comput Phys 1992;100(2):335–54.
[33] Theodorakakos A, Bergeles G. Simulation of sharp gas–liquid interface using VOF method and adaptive grid local refinement around the interface. Int J Numer Meth Fluids 2004;45:421–39.
[34] Nikolopoulos N, Theodorakakos A, Bergeles G. Three-dimensional numerical investigation of a droplet impinging normally onto a wall film. J Comp Phys 2007;255:322–41.
[35] Jasak H. Error analysis and estimation for finite volume method with applications to fluid flows. Ph.D. thesis, Department of Mechanical Engineering, Imperial College of Science, Technology and Medicine, University of London; 1996.
[36] Patankar SV, Spalding DB. A calculation procedure for heat, mass and momentum transfer in three dimensional parabolic flows. Int J Heat Mass Transfer 1972;15:1787–806.
[37] Rhie CM, Chow WL. Numerical study of the turbulent flow past an isolated airfoil with trailing edge separation. AIAA J 1983;21:1525–32.
[38] Ubbink O, Issa RI. A method for capturing sharp fluid interfaces on arbitrary meshes. J Comput Phys 1999;153(Issue 1):26–50.